Proceedings World Geothermal Congress 2020+1
Reykjavik, Iceland, April - October 2021

High Altitude, Iron-Carbonate, Subaqueous Hot-Spring Precipitates of the Central Andes, Peru

Diana Pajuelo[1], Michael C. Rowe[2] and Kathleen A. Campbell[2]

[1]Av. El Sol 662, Lima 35, Peru, [2]Department of Geology, University of Auckland, Auckland, New Zealand

dpajueloaparicio@gmail.com, michael.rowe@auckland.ac.nz, ka.campbell@auckland.ac.nz

Keywords: Iron-carbonate Precipitates, Metals, Central Andes, Peru

ABSTRACT

The Jaraña hot springs are located in a highland (>4570 m), back-arc environment in the southern Peruvian Andes, 90 km east of the present day volcanic front of the Central Andes. The Jaraña geothermal system is controlled by local structures and is hosted within silicified Miocene andesite lava that surrounds the valley containing hot springs and their precipitates. Hot springs occur as thermal pools of varying depths (5cm to 2m) with orange and red precipitates visible below the water surface. Previous geologic studies in the region have identified Cu-mineralization in drill core, suggestive of Cu-ore bodies at depth. In order to assess the potential interactions between the modern geothermal system and potential Miocene mineralization, this study examined the mineralogy and geochemistry of the subaqueous hot-spring precipitates.

The subaqueous precipitates are banded and display nodular and colloform morphologies. The layers contain scattered domical shapes built by convex laminations. Furthermore, the laminations show markedly different colours (black, orange, white) and lustre (metallic, vitreous), clearly suggestive of mineralogical and compositional diversity. X-ray diffraction patterns indicate a mixture of calcite and Fe-oxides. Petrographic analysis indicates calcite crystals, polymictic rock fragments, microbial filaments and diatoms. Cathodoluminescence was used to identify different stages of carbonate deposition, horizons of crystallization, and carbonate fragments. Four-acid digestion results show an inverse relationship between Fe and Ca concentration, consistent with varying proportions of Fe-oxide and carbonate material. Furthermore, in situ chemical analysis of individual horizons by laser-ablation ICPMS contributed to identifying variations in silica in vitreous horizons, abundances of Fe, Zn, Pb and Mo and the relation between them in carbonate layers. In addition, the banded horizons contained high levels of As ranging from 174 ppm to 7.12 wt%. Also, samples have variable concentrations of Cu (0.2 – 268 ppm) and show a positive correlation with base metals such as Zn. However, in samples with high Fe concentrations, Cu is uncorrelated to Fe. This research demonstrates that the Peruvian iron–carbonate subaqueous precipitates contain metal concentration in distinct compositionally laminated horizons. Finally, trace element and metal enrichments in the iron–carbonates may indicate interaction with deeper Cu ore bodies.

1. INTRODUCTION

Hot spring deposits are surface manifestations located around continental active hot springs vents within geothermal systems. Chemical compositions of the ensuing precipitates generally fall into two types of lithologies: sinter (silica based, opaline silica) and travertine (carbonate based, calcite or aragonite) (Renaut & Jones, 2000). In addition, sinter and travertine could be mixed and generate sinter-carbonate deposits (Campbell, Rodgers, Brotheridge, & Browne, 2002; Smith, 2008). When thermal waters are saturated in Fe (II), Fe (III) (oxide-hydroxides or ferrihydrite) deposits may accumulate at the surface, under oxidizing conditions. Hydrodynamic variation generates subaerial or subaqueous deposition, which produces various morphologies of hot spring deposits (e.g. Pentecost A., 2005; Campbell et al., 2015). Hot spring deposits contain a record of physical characteristics such as colour variation caused by a predominant element concentration, and layering thickness with various forms (parallel or wave) caused by flow rate vs. evaporative conditions and fluid volume. Moreover, hot spring deposits can entomb local biota (e.g. leaves, insects, microbes) during rapid precipitation (Lynne & Campbell, 2003; Lynne, 2012; Guido & Campbell, 2018). In particular, the thermal environment hosts microbial communities of mats and biofilms often expressed as colourful covertures (e.g. green, orange) above surface manifestations (Stolz, 2000). Common microbial communities in hot spring terrains are cyanobacteria (flourishing in temperatures below about 55ºC) and diatoms (found at temperatures between 30 to 44 ºC) (Brock, 1978). The microorganisms generate metabolic activities and secrete extracellular polymeric substances (EPS) appropriate for nucleation and mineral saturation (Renaut & Jones, 2000). However, the mineral deposition could also be induced by abiotic factors (Handley, Campbell, Mountain, & Browne, 2005).

Globally, the trace element concentrations of precious metals (Au, Ag) and base metals (e.g. Cu, Pb, Zn) in sinter and travertine are related to ore mineralizing processes at depth (Cunneen & Sillitoe, 1989; Fournier et al., 1994; Guido et al., 2002; Lynne et al., 2005; Guido et al., 2010; Hayashi, 2013; Nicolau, 2013; Hamilton et al., 2017; Kanellopoulos et al., 2017; Campbell et al., 2018; Hamilton et al., 2019). In effect, studies revealed that hot spring deposits contain precious and base metal concentration correlated with iron and arsenic elements. For example, Fournier et al. (1994) reported that sinter in Yellowstone National Park (United States) contains precious and base metal elements with moderate iron (0.005 to 1.40 wt%) and arsenic (100 to 1120 ppm) concentration. Nicholson & Parker (1990) reported that sinter at Atiamuri, Champagne Pool, Ohaaki Pool, and Tokaanu Springs (New Zealand) contains base metal elements associated with concentrations of iron in the range of 0.14 to 0.71 wt%, and arsenic in the range of <1 to 246 ppm. Nicolau (2013) reported that sinter at El Tatio (Chile) contains base metals correlated with Fe_2O_3 in the range of 0.01 to 18.8 wt% and arsenic in the range of 5 to >2000 ppm. Furthermore, Kanellopoulos et al. (2017) reported that travertine from Northern Euboea Island and Sperchios (Greece) contains base metal elements related to iron concentration in the range of 0.01 to 28.9 wt% and arsenic in ranging from 66 to 18300 ppm. Therefore, Fe and As could be an indicator for base metal concentration in hot spring deposits.

Indeed, hot spring deposits (sinter and travertine) represent a surface manifestation of geothermal system and a quiet phase of volcanism (Guido & Campbell, 2011), where meteoric water infiltrates through rocks and fractures, fluids interact with magmatic sources, trap volatiles and elements, and ascend through surface as convective cells (Renaut & Jones, 2011). During the ascending process fluids interact with rocks, contain trace elements from depth and precipitate on the surface as sinter or travertine with other saturated elements (Rowland & Simmons, 2012).

The Jaraña hot springs in the southern Andes of Peru are at high altitude (>4000 msnm), with thermal water discharge through Miocene andesite lavas exhibiting advanced argillic alteration and silicification. Core drill samples in the north area of the hot springs revealed that andesitic rocks contain copper sulphide and sulfosalt minerals; mineral characteristics suggest a porphyry copper mineralization at depth (Valdivieso, 2015). Thermal waters discharge (55 - 74 ºC) with neutral pH and alkali-chloride and acid sulphate composition (Cruz, 2016). The saturation of elements allows calcite and gypsum mineral precipitation with other minerals enriched in elements such as Ag, Cu, Pb, As, Sn and Fe (Pajuelo, Condorhuaman, Cruz, & Zegarra, 2016). Spatial analysis suggests the interaction of geothermal fluids with sulphide copper minerals in the host rocks, and hot spring precipitates could incorporate base metals.

2. GEOLOGICAL SETTING

Peru is located along the subduction boundary between the Nazca and South American plates. The angle of subduction of the Nazca Plate in southern of Peru is ~30º ("normal angle"), promoting active volcanism (Figure 1); the Nazca ridge affects the angularity of subduction (Gutscher, Olivet, Aslanian, Eissen, & Maury, 1999). Nazca ridge migration over time generated various ore deposits along the length of Peru (Rosenbaum et al., 2005), and the evolution of the Andes mountains allowed their actual exhumation (Tassara, 2005). Nowadays, the active subduction zone generates hot springs along the Central Andes at high altitudes over the exhumed ore deposits (Figure 1).

The Pinaya geothermal field is a group of hot springs located close to homesteads (e.g. Pinaya, Atecata, Jaraña and Jarpaña) at Lampa Province, in the Puno region, southern Peru. The Puno region is part of the high plains or Altiplano, and hot springs are active at high altitudes over 4570 meters. The group of hot springs is located 90 km to the east of the active volcanic arc in the Sillapaca Cordillera. These mountains have northwest to northeast trend (>5000 m peaks) and divide the area of active hot springs into western and eastern zones. The Pinaya and Atecata hot springs are located in the western zone, and the Jaraña and Jarpaña are found in the eastern zone.

The Jarpaña hot springs are structurally influenced by local faults related to regional faults (Cusco-Lagunillas-Mañazo fault) which, in turn, expose old rock units. The oldest rocks are Cretaceous sandstones (Hualhuani Formation) and limestones (Arcurquina Formation), overlain by Paleocene–Eocene red-bedded sandstones and conglomerates with a calcareous matrix (Puno Group). A volcanic Cenozoic sequence overlies the folded older rock units and consists of andesitic lavas (Tacaza Group), white tuffaceous deposits (Palca Group), lacustrine units interbedded with volcaniclastic deposits (Maure Group), and andesitic to basaltic lava (Sillapaca Group). The Cenozoic volcanic rocks were intruded by tonalitic and granodioritic rocks (25.7 Ma), andesitic to basaltic rock lavas (19 Ma) and a dome shaped subvolcanic rock unit at Pinaya with a geochronological age of 0.842 Ma. Specifically, hot springs at Jaraña are surrounded by andesitic to basaltic-andesitic rocks (Sillapaca Group) affected by hydrothermal alteration (argillic-advanced argillic) and silicification. The rocks on the northern side of the Jaraña hot springs contain sulphide minerals such as pyrite (FeS_2), rutile (TiO_2), arsenopyrite (FeAsS), enargite (Cu_3AsS_4), luzonite (Cu_3AsS_4), covellite (CuS), digenite (Cu_9S_5) (Valdivieso, 2015). Moreover, iron minerals such as hematite (Fe_2O_3), limonite ($FeO(OH).nH_2O$) and jarosite are associated with the copper minerals identified during exploration core drilling in the Sabina mineral project (Valdivieso, 2015). The analysis is focused on the Jaraña hot springs because of their particular location over a mineralized area (Figure 1).

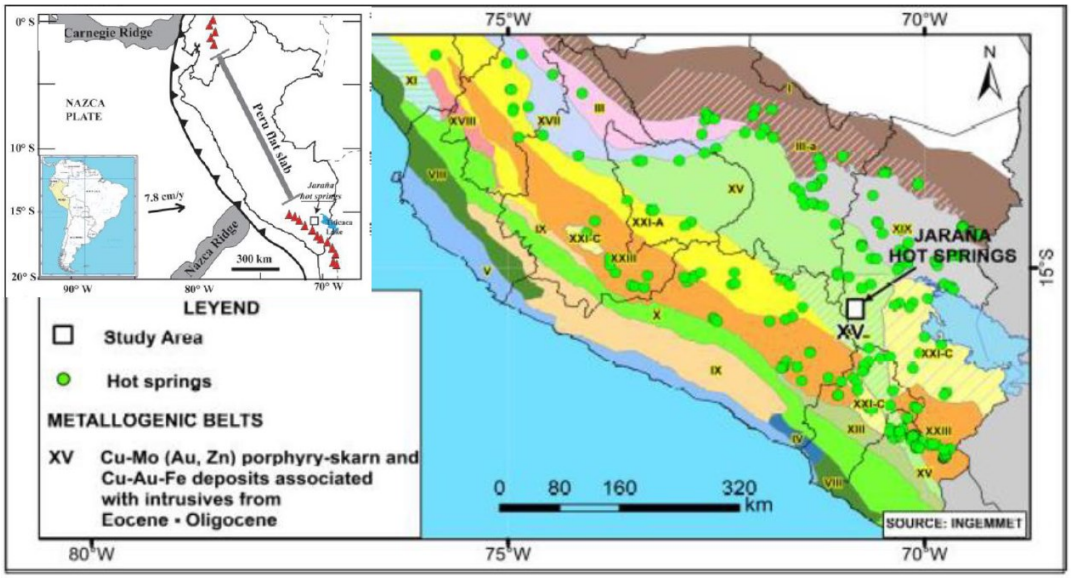

Figure 1: Location map of Peru with hot springs above exhumed ore bodies and Jaraña hot springs area (INGEMMET, 2018).

3. JARAÑA HOT SPRING AREA

Jaraña comprises a group of hot springs distributed along a flat valley. Hot springs emerge from the ground and generate thermal pools and streams of variable depths (~5cm to 2m). Thermal water has a nearly neutral pH (6-6.7) and water temperatures at surface range from 55 to 74 ºC. Thermal waters have an alkali-chloride and acid sulphate composition (Cruz, 2016). Some elements such as Na, Ca, Cl, SO_4, HCO_3 and SiO_2 have concentration above 100 mg/L, while other trace elements such as Li, F, B, As, Sr, Fe, Rb, Cs and Mn register concentrations between 0.1 and 10 mg/L (Cruz, 2016). Moreover, the active hot springs precipitate deposits above and below the water surface (subaerial and subaqueous, respectively). Previous studies (Pajuelo et al., 2016) revealed that hot spring precipitates contain minerals such as calcite, halite and gypsum, and other minerals enriched in Ag, Cu, Pb, As, Sn and Fe.

Subaqueous hot spring deposits at Jaraña are orange to red in colour and display three main features in relation to thermal pool depth. Firstly, deep thermal pools (~1-2m) contain hot spring deposits with rounded to dome-like shapes (Figure 2A). Secondly, thermal pools at shallow depths (5-30cm) contain hot spring deposits with irregular discoidal shapes, with shallow, bowl-shaped depressions surrounded by a rim of hardened precipitate (Figure 2B). Finally, these orange deposits can precipitate as small spring conduit mound in shallow water; the mounds (~10 cm diameter) are circular with cylindrical central holes (Figure 2C). Generally, orange and green mats extend over the water surface or cover the conduit mound deposits. Some of the subaqueous hot spring deposits disaggregate into small massive fragments when they are removed from the water; fragments may contain polygenetic grains.

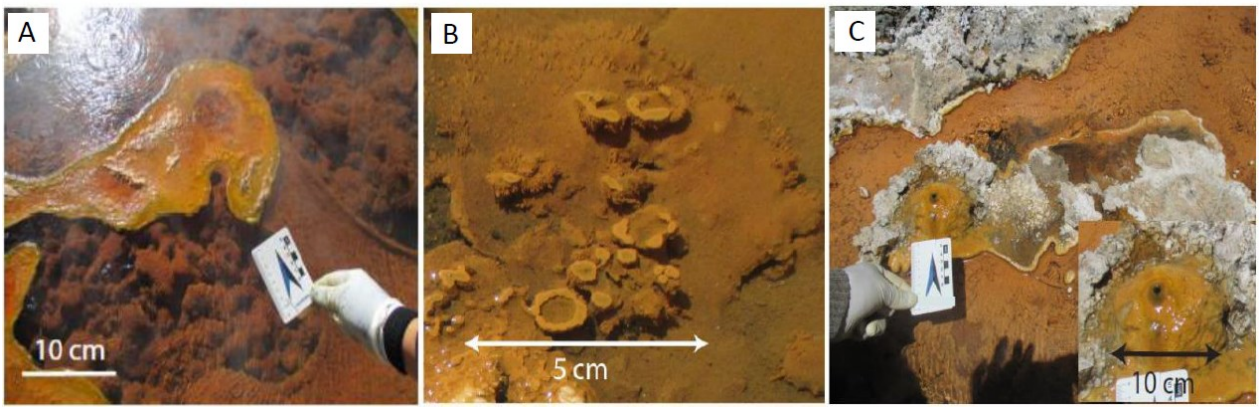

Figure 2: Jaraña subaqueous hot spring deposits have A) rounded to dome-like shapes with orange and green mat floating on the surface, B) irregular discoidal shaped with shallow, bowl-shaped depressions surrounded by a rim of hardened precipitate, C) spring conduit mound in shallow water.

4. METHODS

A total of 25 bulk rock samples were collected from subaqueous precipitates in and around thermal pools and/or streams. Samples were cleaned and described according to their morphological characteristics. Then, samples were analysed using laboratory methods such as X-ray diffraction (XRD), Scanning Electron Microscopy and Energy Dispersive Spectroscopy (SEM-EDS), optical microscopy, cathodoluminescence and Laser Ablation Inductively Coupled Plasma Mass Spectrometry (LA-ICP-MS) at University of Auckland, New Zealand, and via the acid-digest method using ICP-MS and ICP-AES at ALS laboratories (Vancouver, Canada).

XRD analysis was used to determine the mineralogy of samples. Samples were extracted with a spatula from different coloured layers and hand milled using an agate mortar and pestle. The powdered samples were analysed in four batches using a PANalytical Empyrean X-ray Diffractometer with a silica standard as a reference and a 2-degree anti-scatter slit. The diffraction patterns were processed, and minerals identified with High Score Plus software.

SEM-EDS was used for microtexture identification at the Research Centre for Surface and Material Science, University of Auckland. Samples were affixed onto pin mounts using carbon tape and carefully orientated, photographed and double-coated with platinum utilizing a Quorum Q150R S vacuum cycle for 10 minutes. Then, samples were analysed with an XL30 S-FEG Philips instrument with an accelerating voltage of 5, 20 and 30 kV, a beam current of <1 µA and 1.5 nm of resolution. Also, samples were analysed with a Quanta 200 instrument using an average pressure of 0.60 Torr, an accelerating voltage of 10 and 20 kV, a beam current of <1 µA, and resolution of 3 nm. EDS compositional data were collected upon a flat surface on the samples. Optical microscopy was undertaken on representative samples cut at transverse and longitudinal orientations with respect to the land surface. Some samples were prepared at the University of Iowa because of their easy disintegration in water while other samples were prepared at the University of Auckland (Earth Science processing Lab). Sample preparation required vacuum impregnation with epoxy. Petrographic observations were made on Nikon eclipse LV100POL microscope and thin section mineral descriptions were based on optical properties. Thin sections were also analysed using an optical cathodoluminescence (CL) microscope for carbonate identification. The CL instrument has a CITL CL Mk5.2 electron beam source and was operated at 15kV and 350 µA. Samples were exposed to the electron beam source between five to ten minutes.

Major and trace element geochemistry of samples was determined by LA-ICP-MS and 4-acid digest. LA-ICP-MS was conducted on an Agilent 7700 ICP-MS instrument coupled with a 193 nm New Wave Excimer laser ablation system. The laser beam energy was ~7 J/cm^2 with a beam diameter of 75 µm. A rep rate of 5 Hz with an ablation time of 60 seconds, followed by 45 seconds of washout time, was utilized for all samples. Standard calibration was undertaken using GSE-1G, with GSD-1G as a secondary standard. LA-ICP-MS was primarily used for determining the trace element abundances between horizons, too small to be sampled for the 4-acid digest. For the 4-acid digest method, samples were milled and powdered (0.5 grams). Samples were dissolved using 4-acid digestions (HNO_3, $HClO_4$, HF and HCl) and the final solution was analysed by inductively coupled plasma-mass spectrometry (ICP-MS) and

inductively coupled plasma-atomic emission spectrometry (ICP-AES). The 4-acid digest and analysis method utilized here by ALS reports 48 elements and 12 rare earth elements.

5. RESULTS

5.1 Morphology

Subaqueous hot spring deposits at Jaraña occur as small fragments with or without varied morphologies and textures. Small massive fragments are orange and may contain acicular crystals or polygenetic grains. Moreover, some fragments of hot spring precipitates have varied nodular morphologies and textures with banded horizons. Nodular morphologies are variably elongated. The nodules appear as columns (0.2 to 0.5 cm high) with spherical terminations, and a rounded base ranging from 0.1 to 0.2 cm wide. Spherical nodules contain circular laminae (Figure 3A). Some of the columns are laterally linked and some of the spherical shapes have a weathered nucleus at the top. The crowded manner of nodules produces a cauliflower–like morphology (Figure 3B). Nodules grow in laminated horizons with variable thicknesses, a wide range in colours (e.g. orange, red, white, grey, black or white) and different lustre types (e.g. opaque, vitreous or metallic). Thickness varies from millimetric to centimetric size. Laminations cover or trap concave-shaped fragments. Generally, fragments are found at the base of samples or initial phases of deposition, with red colours and uniform porosity; their sizes vary from 1.1 x 0.7 cm to 4 x 3 cm (Figure 3A). Also, subaqueous deposits have colloform textures and often are part of spring conduit mounds, where the rounded surface are built by rhythmic precipitation, surfaces are smooth and convex and contain laterally continuous, wavy laminations (Figure 3C).

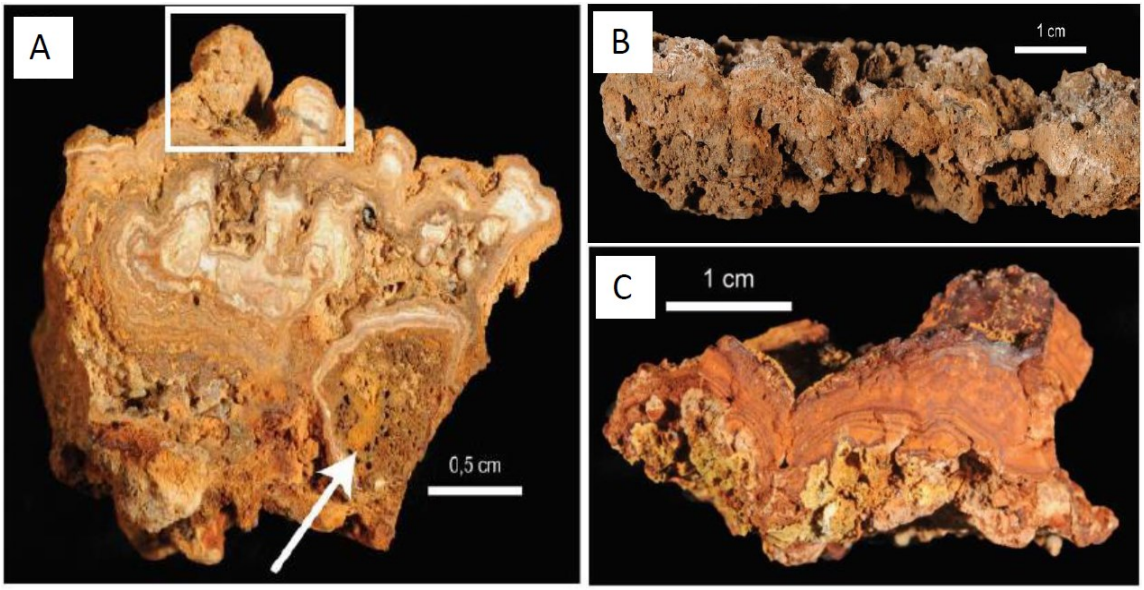

Figure 3: Subaqueous hot spring deposits with varied morphologies: A) nodules with columnar growth and laminated horizons: white arrow shows a porous fragment, B) laterally-linked nodules, C) colloform texture with rhythmic precipitation.

5.2 Mineralogy

X-ray diffraction patterns show heterogeneous mineralogy in the subaqueous precipitates yielding calcite, small proportions of iron-oxides (Figure 4) and a low amount of manganese-oxide. Massive fragments and nodular morphologies in hot spring deposits commonly contain iron-minerals such as hematite (Fe_2O_3), goethite (FeO(OH)), magnesioferrite ($MgFe^{3+}{}_2O_4$) and franklinite ($ZnFe^{3+}{}_2O_4$). Other secondary minerals are incorporated in small proportions such as halite (NaCl), alabandite (MnS), gypsum ($CaSO_4.2H_2O$) and lime (CaO), which are not found in all subaqueous deposits. Nodular morphologies with irregular discoidal shapes contain hematite (Fe_2O_3), goethite (FeO(OH)), magnesioferrite ($MgFe^{3+}{}_2O_4$) and franklinite ($ZnFe^{3+}2O^4$) in moderate proportions and manganese-oxide in small proportions. The spring conduit mounds contain minor mineral phases of ilmenite ($FeTiO_3$) and magnetite (Fe_3O_4) minerals, as well as small amounts of phases such as magnesite ($MgCO_3$) and sulphides minerals enriched in silver and arsenic.

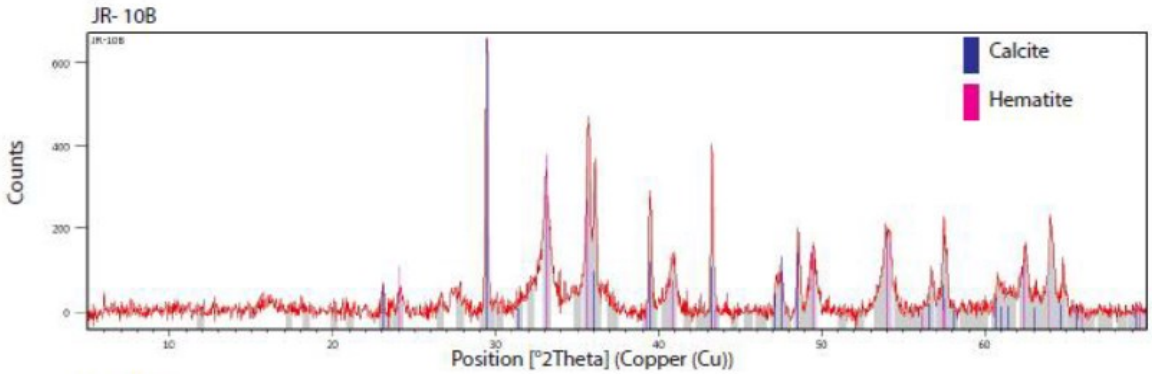

Figure 4: X-ray diffraction patterns for calcite and Fe-oxide (hematite).

5.3 Microtextures

A microscope and SEM-EDS analysis showed the texturally complex nature of the subaqueous precipitates (Figure 5). The massive fragments contain acicular crystals, and SEM images detected a cluster of spherical morphologies above the acicular surface. Nodular and botryoidal morphologies with laminated horizons contain crystals, polymictic clasts and microorganisms. A predominance of calcite crystals occurs in the nodular laminated horizons compared to the laminated botryoidal morphologies; therefore, nodular morphologies contain more carbonate horizons compared with botryoidal morphologies. The calcite crystals have grainy, acicular and fragmented calcite shapes and are of variable sizes (~100-800 µm).

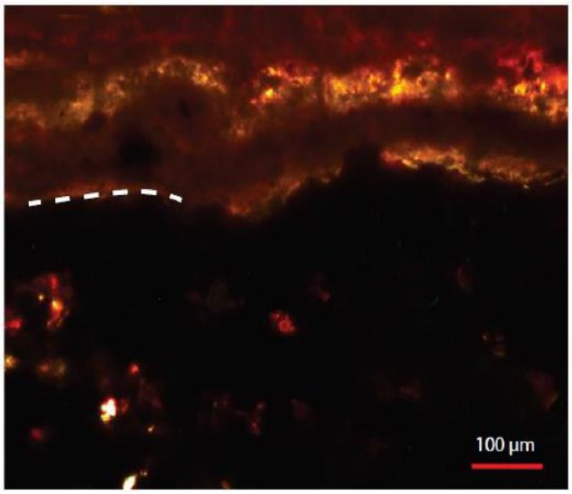

Figure 5: Dashed white line represents the boundary between Fe-rich laminated horizons and porous fragment.

Grainy calcite crystals increase in size in colloform morphologies. Acicular crystals may form as fan shaped microtextures and are randomly distributed inside some laminated horizons. Moreover, fragmented crystals may contain secondary black cement filling the joints between crystals, which are rich in manganese based on EDS analysis. SEM analysis showed that carbonate horizons contain tabular crystals with sharp edges covered by two different carbonate cement types: spherical and spiky. EDS analysis detected enrichment of the carbonate in elements such as Fe, As, Si and Na. The calcite crystals may be interbedded with orange to red cemented horizons with aphanitic texture under the microscope. The orange laminated horizons have a carbonate composition with high concentrations of Fe, moderate amounts of Si, and trace amounts of Ca, As and Mn. Also, the high concentration in oxygen (23.76 wt %), seems to indicate the precipitation of iron-oxide minerals.

Reflected light microscopy showed that laminated horizons are good hosts for disseminated opaque minerals. Opaque minerals in carbonate horizons occur atop the matrix randomly distributed or disseminated inside layers and are small in size (~10 µm in diameter). Reflected light microscopy indicates the presence of pyrite and copper minerals. Carbonate horizons contain isotropic anhedral crystals with pale yellow colours which suggest iron sulphide such as pyrite. Iron-rich horizons contain a large (~50 µm in diameter), anhedral mineral with yellow, pink and blue colours and no pleochroism (Figure 6A). These optical properties suggest the presence of a copper sulphide mineral. The small opaque crystals (15 µm) under the SEM are shiny crystals overlying a calcareous matrix where four opaque minerals were identified. The first is a mineral with platy crystal habit that forms bunches of plates along a filament (Figure 6B). EDS analysis indicated that the platy crystals comprise a mixture of carbonates and oxides mainly enriched in Fe, moderately enriched in Ca, Mn, Si and Sr, and with traces of As, Na, Al and K. The second is a mineral with small platy crystals; EDS identified the composition as a Sr-bearing mineral enriched in Fe and Ca and with traces of As, Si, Mn, Ba, P and Na. The third is a crystal with a pseudo-octahedral shape, whereby the EDS indicated a Fe-oxide mineral with traces of As, Si, Sr, Al, Mn, P, Na and Ba. The fourth is a crystal overlying the pseudo-octahedral crystal and comprising a clustering of spherical shapes,

similar to a framboidal texture (Figure 6C). The framboidal mineral is mainly enriched in Fe and Cu; it also has low concentrations of Sr, Ca, As, Si, Al, Na and Mn and low concentrations of C, O and S anions.

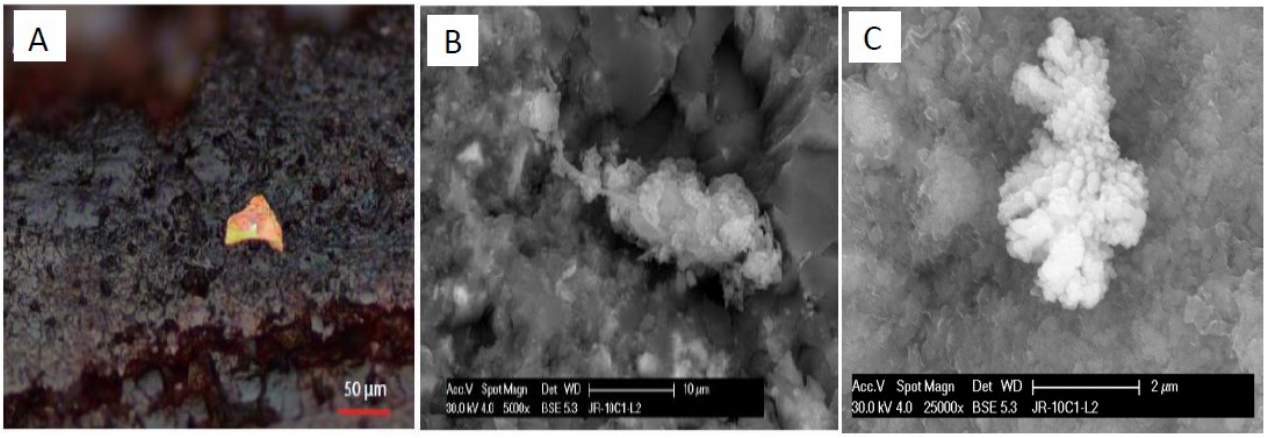

Figure 6: A) Iron rich layer horizon with an opaque mineral, B) platy crystal habit along a filament line, C) pseudo-octohedral crystal with a framboidal mineral.

Furthermore, laminated horizons contain randomly distributed, heterogeneous clasts with variable shape and size. The clasts may appear above crystal surfaces joined by a calcareous cement. Also, carbonate and iron-rich, red laminated horizons may contain diatoms and filaments, especially in iron-rich horizons. Diatoms are boat shaped, and filaments appear in red horizons forming criss-cross shapes with knots along with their extension (Figure 7). The heterogeneous clasts and microbial communities vary laterally and horizontally between each laminated horizon. Where laminated horizons contain more iron-rich cement, precipitation trapped convex–concave-shaped fragments (diatoms), and the depositional process incorporates small clasts into the deposit's structure. The fragments mainly contain transparent filaments with irregular wavy surfaces.

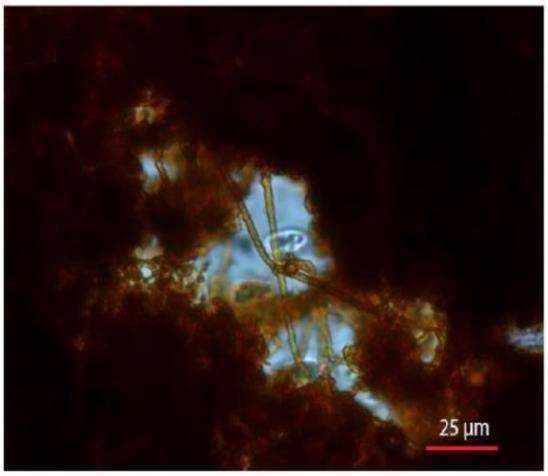

Figure 7: Iron rich horizon with criss-crossed filaments.

5.4 Carbonate precipitation

The results using cathodoluminescence indicated that carbonate precipitation is frequent in subaqueous deposits. CL analysis allowed identification of carbonate in laminated horizons, with bright orange luminescence indicating manganese or iron. Iron (Fe) has an important (high) concentration in hot spring deposits according to EDS results; thus, Fe quenches the luminescence of CL brightness. The CL pattern indicated no to dull dark luminescence in samples with iron-rich horizons in the spring conduit mounds with colloform morphologies. Subaqueous precipitates with predominantly carbonate horizons show thin lamination with dark orange luminescence at the base and a light orange CL in upper sequences. The differences in brightness orange luminescence reflect slightly different fluid compositions during precipitation, which varies from secondary iron-carbonate to manganese carbonate sequences. The variation between iron and manganese may reflect the high and moderate concentration on precipitates. The sequences represent depositional and diagenetic process (Figure 8A). The iron carbonate horizons contain cavities that are filled with carbonates which show a light orange luminescence, which indicates that cavities were filled with manganese carbonate precipitation (Figure 8B).

The nodular morphology contains an orange luminescence which underlines the nodule growth, the nodule builds up with continuous carbonate sequences forming convex laminated groups and is later covered by a thin carbonate layer. Botryoidal morphologies registered orange to light orange luminescence, which represents the successive calcite crystal growth, interbedded with manganese-

oxide mineral lamination. The inner area has a lighter orange luminescence and contains small cavities filled with carbonates enriched in iron (dark orange colours).

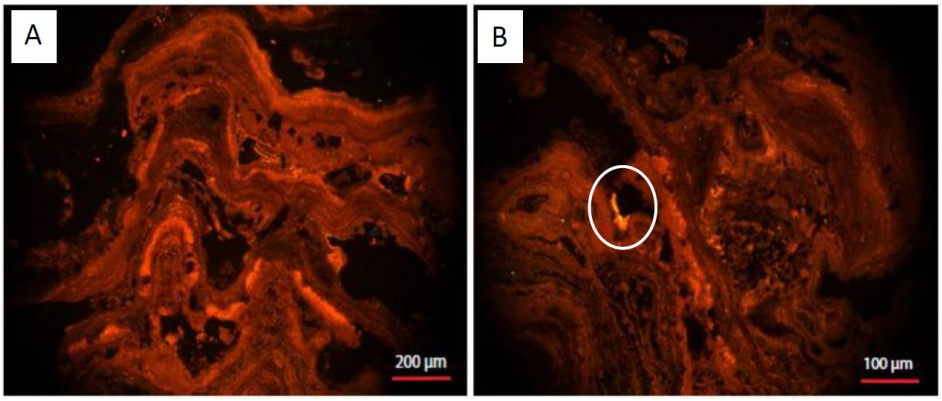

Figure 8: A) Variable orange colour luminescence shows different stages of carbonate precipitation, B) Cavities contain later carbonate precipitation rich in manganese.

5.4 Geochemistry

The geochemistry is variable in the samples because of the different layers in the subaqueous deposits. LA-ICP-MS and 4-acid digest results identified that layer horizons can also contain anomalous concentrations of Si (63.3 wt%), Fe (34.5 wt%) and As (>10000 ppm). The increase in Si relates to low Fe and As concentrations (Figure 9A). In contrast, high Fe concentration relates to low Ca amount. Anomalous As concentrations occur where Fe precipitates as an iron-oxide mineral (Figure 9B).

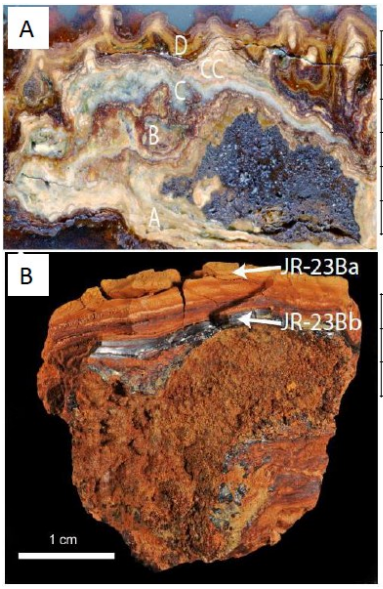

Horizon	Si (Wt%)	Fe (Wt%)	As (ppm)
A	67.8	0.83	587
B	23.3	6.88	6968
C	63.3	2.47	2727
CC	31.0	1.48	1176
D	10.6	3.23	3489

Horizon	Ca (Wt%)	Fe (Wt%)	As (ppm)
JR-23Ba	3.91	27.5	>10000
JR-23Bb	2.77	34.5	>10000

Figure 9: A) Laminated horizons (A, B, C, CC and D) in subaqueous deposits and concentration of Si, Fe and As; B) Laminated horizons (JR-23Ba and JR-23Bb) in subaqueous deposits and measured Ca, Fe and As abundances.

5.4.1 Trace elements in Jaraña hot spring deposits

Trace element concentrations were obtained from 21 bulk samples (4-acid digestion) and 148 spots from laminated horizons (LA-ICP-MS). The results indicate that subaqueous deposits contain a high concentration of Ca, Fe and Si (>0.1 wt%). Ca and Fe values have an inverse proportion between them. Moreover, subaqueous hot spring deposits contain variable Al (0.01 to 10 wt %), with a similar overall range to As (174 ppm to 7.12 wt%). Mn and Sr have concentrations <1 wt %, similar to Na, K and Mg results. Analysis of Fe and As showed that they co-precipitate in the subaqueous hot spring precipitates but only if Fe amounts are <10 wt% (Figure 10A). Those subaqueous precipitates with Fe concentrations >10 wt% have no apparent influence on As precipitation/concentration. Furthermore, a comparison of Fe and Si abundances shows that subaqueous precipitates with Si concentrations <10 wt% are positively correlated, but if Si concentration is >10 wt% the correlation between Fe and Si may form a negative trend (Figure 10B). This might

suggest that above 10 wt% for major cations (SiO_2 and FeO) we see a shift in the behaviour governed by changes in the primary mineralogy.

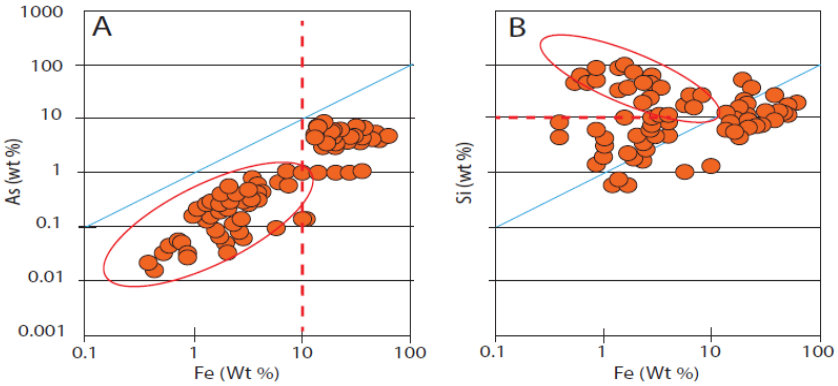

Figure 10: Binary diagrams (wt%) from LA-ICP-MS and 4-acid digest data, analysis between A) Fe vs As, red circle demarcates positive trend; B) Fe vs Si, red circle indicates a negative trend. Red dotted lines delineate the 10 wt% value.

Other trace elements (Cs, Be, U, Mo, W, Cd, Tl, Ge and Sb) showed a positive correlation when they interact between them. Particular cases include Co, Ni, Cu, Zn and Pb, which showed variability in concentrations, probably because of the rhythmic laminated horizons in subaqueous hot spring precipitates. Base metals such as Cu (0.03 – 333 ppm) and Zn (173 – 71204 ppm) were in high concentrations in subaqueous deposits with carbonate and iron rich layers; whereas, Pb concentration was high (0.12 – 308 ppm) only in iron rich laminated horizons. Furthermore, anomalous concentrations of REEs (0.01 to 1 ppm) occurred in laminated horizons with high Fe concentration (>1 wt%). In contrast, Ag registers the lowest values (<0.002 - 0.06 ppm). The analysis between Zn and Ni show a strong positive correlation. However, subaqueous deposits with predominantly Fe-rich laminated horizons form two trends of a positive correlation between Zn and Ni (Figure 11A). Similarly, the analysis between Zn and Cu showed a positive correlation for subaqueous deposits where laminated horizons alternate between carbonate and iron composition. The increase of subaqueous deposits with Fe produces the scattered plots reflecting the mobility of Cu during Zn precipitation (Figure 11B). The analysis of Zn and Pb showed a positive trend for subaqueous precipitates; however, plots have a scattered behaviour (Figure 11C). Therefore, Zn is one of the base metal elements that show an affinity for a positive correlation and Fe precipitation in controlling Zn, Cu and Ni abundances, although the affinity varies with horizon composition.

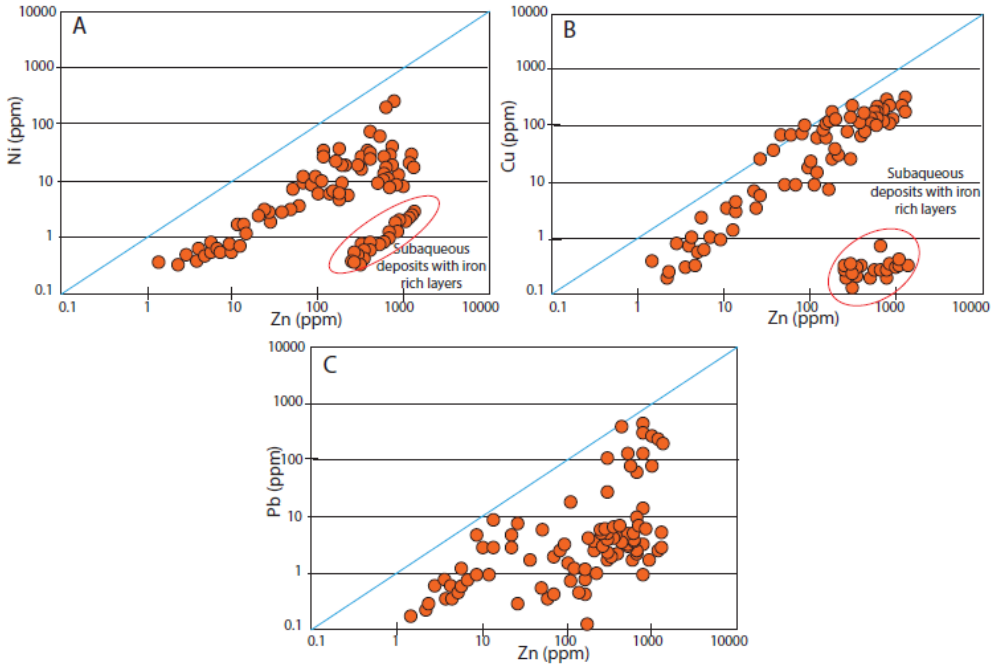

Figure 11: Binary diagrams (ppm) from LA-ICP-MS and 4-acid digest data, analysis between A) Zn vs Ni; Zn vs Cu; C) Zn vs Pb. In red circles plots from subaqueous hot spring deposits with iron-rich laminated horizon.

6. DISCUSSION

6.1 Iron-carbonate deposits

The dominance of calcite and iron-oxide mineral (and corresponding high concentrations of Ca and Fe) in subaqueous hot spring precipitates at Jaraña lends support for the terminology of an iron-carbonate precipitate. Similarly, laminated horizons contain hematite likely caused by ferrihydrite precipitation under the influence of iron-oxidizing bacteria (Kanellopoulos et al., 2017; Takashima et al., 2011). However, Jaraña subaqueous precipitates also contain siliceous laminated horizons with high Si concentrations; however, siliceous layers are uncommon.

A comparison with other hot spring deposits with economic metal concentrations indicates similar low Ag concentrations in Jaraña Fe-carbonate deposits (<0.002 - 0.06 ppm) and Savo volcano travertine deposits (0.003 - 0.04 ppm) in the Salomon Island (Smith, 2008). Cu has a variable and low range in concentrations at Jaraña (0.03-333 ppm) compared to the sinter deposits at El Tatio (Chile), where Cu has a high concentration (420 - 20528 ppm) in sinters (Landrum et al., 2009). Similarly, the high concentration of Pb (0.12 - 308 ppm) at Jaraña is generally greater compared to other travertine or mixed deposits, except for sinter deposits at El Tatio, Chile, which registers a greater concentration of Pb (2398 - 7293 ppm). The high concentration of Cu and Pb in sinter deposits at El Tatio (Chile) relates to the high Sr amount (64.8 - 315 ppm) (Landrum et al., 2009). It is relevant to mention the high Zn concentration at Jaraña (173 - 71204 ppm) compared with other cases of travertine or sinter. El Tatio sinter shows a high amount of Zn (<30 - 410 ppm) but these are lower compared with Jaraña Fe-travertine precipitates. The anomalous concentrations of Zn could have a relation with high As amount (173 - 71204 ppm) at Jaraña, similar with travertine cases with high As (66-18300 ppm) concentration at Northern Euboea Island and Sperchios (Greece) (Kanellopoulos et al., 2017).

6.2 Metal crystallization

Carbonate laminated horizons may form cavities generated by carbonate dilution and generate spaces for mineral crystallization (Kanellopoulos et al., 2017). Fe-carbonate laminated horizons in Jaraña hot spring deposits act as a good host for a late mineral crystallization and contain oxide and sulphide minerals as crystals inside cavities as part of the last crystallization stage. Moreover, the Fe-oxide minerals are good hosts to induce the Fe-Cu sulphide grainy crystallization (framboidal textures). From this, it seems that base metals (Cu in this current work) can crystallize over a Fe-oxide mineral crystal surface. Furthermore, travertine can host oxide and sulphide minerals as seen in Greece and Russia (Okrugin, Andreeva, Chubarov, Yablokova, & Shishkanova, 2015; Kanellopoulos et al., 2017;).

6.3 Mineral precipitation and microbial influence

Hot spring deposits form from both abiotic and biotic processes, with microbes commonly serving as templates upon which minerals precipitate (Handley et al. 2005). At Jaraña, the hot spring precipitates contain microorganisms (diatoms and filaments) around which authigenic minerals nucleate. The orange and green microbial mats floating within and over the thermal water surface contain minerals in their EPS. Boat shaped diatoms are similar in morphology to *Surirella* species (Bramburger, Haffner, Hamilton, Hinz, & Hehanussa, 2006) and may reflect the Si precipitation during the rhythmic laminated horizons. Takashima, Kano, Naganuma, & Tazaki (2008) found that filaments increase in abundance under high Fe concentrations and a decrease in filaments (i.e., drop in Fe content) contributes to carbonate precipitation; the variation of diatoms and filaments in horizons may reflect the variability of Fe and Ca amount. Also, Fe and Cu mineral crystallization found in carbonate pore spaces in Jaraña hot spring deposits could have relation with biotic and abiotic factors; thus, the microbial metabolism produces ligands and generates crystals (biotic factors) and dead microorganisms could leave pore spaces amenable to mineral nucleation (abiotic factors) (Ferris, 2000). Additionally, nodular morphologies are built by convex laminations which could be comparable with stromatolites or thrombolite macrofabrics, commonly found in evaporitic and calcareous environments (Alshuaibi & Khalaf, 2015; Terra et al., 2010; Warren, 2016).

6.4 Diagenetic events

Diagenetic events of the Jaraña subaqueous hot spring precipitates are indicated by stages of deposition within in the Fe-carbonate laminated horizons. Diagenetic events constitute the following components: large porous fragments trapped on rhythmic lamination (alloctonous fragments), mineralization, polymictic grains, and pore-controlled microbial and mineral deposition in cavities (Figure 12). During the time of deposition, three events were recognized as early, middle and late. An early time constitutes a large trapped porous fragment in rhythmic lamination. The fragment with porosity has a mainly Fe composition, it is incorporated into the Fe-carbonate structure with a greater quantity of filaments and diatoms. Intermediate precipitation includes laminated horizon deposition with Fe-oxide composition, calcite, silica composition and hematite mineral precipitation which alternate randomly as fluids fluctuate. Fe-rich layers are precipitated banded hematite and may be interbedded with calcite; however, Fe-rich layers do not have inter-bedding with silica layer horizons. Laminated horizons contain calcite as grainy, fibrous and fragmental crystals; calcite crystallizes simultaneously with calcite layer precipitation. Polymictic grains are incorporated progressively along the middle time of deposition. Microbial filaments are more abundant during the first stages of Fe precipitation and decrease when silica precipitates, according to with the petrographic analysis in laminated horizons. Diatoms appear when iron, carbonate or silica precipitates. A late time of deposition consists of carbonate dissolution process which allows the presence of cavities convenient for pore filling mineral deposition.

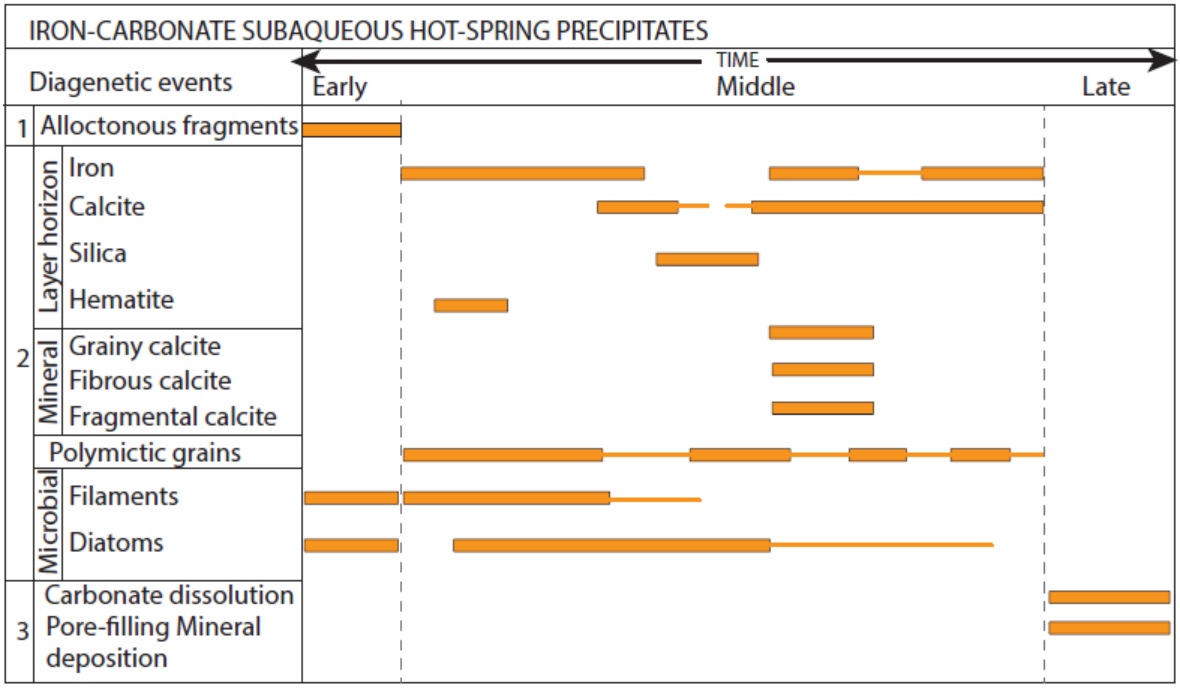

Figure 12: Relative timing relationships and distribution of diagenetic processes for Fe-carbonate subaqueous hot-spring precipitates. The line thickness represents the high and low concentration of components.

7. CONCLUSIONS

The Jaraña hot spring deposits have a main composition of Fe (ferrihydrite) and Ca elements which precipitates as rhythmic laminated horizons and crystallizes as minerals such as Fe-oxide (hematite) and calcite. The carbonate dissolution releases empty pores which are filled by a late deposition of carbonate and oxides as disseminated opaque minerals enriched in Fe, Sr and Cu (platy, pseudooctaedral, framboidal textures) with sizes around 30 µm. The identification of microbial communities (diatoms and filaments) does not show a clear influence for mineral crystallization; however, the nodular built may reflect microbial growth as stromatolite or thrombolite macrofabrics.

The geochemical analysis supports the high Fe and Ca concentrations in subaqueous hot spring precipitates. Fe has a proportional increase with As but not with Si. However, Ca and Si shows compatibility during their precipitation forming laminated horizons. Moreover, the variation in Ca and Fe influences the economic metal concentrations of Cu, Pb and Zn, which are distributed throughout the precipitating phases as incompatible elements with trace amounts.

Finally, the high Fe and Ca amounts in hot spring precipitates are part of calcareous and iron concentrations in rocks at depth (Arcurquina Formation and Puno Group); these elements may be removed from rocks caused by the circulation of geothermal fluids at depth. Similarly, the As, Cu, Zn and Pb trace concentration detected in Jaraña subaqueous precipitates could be part of mineralized rocks (copper sulphide minerals) located at the north side of Jaraña and/or hidden minerals at depth.

REFERENCES

Alshuaibi, A. A., & Khalaf, F. I. (2015). Calcareous thrombolitic crust on Late Quaternary beachrocks in Kuwait, Arabian Gulf. *Arabian Journal of Geosciences*, *8*(11), 9721–9732. http://doi.org/10.1007/s12517-015-1869-5

Bramburger, A. J., Haffner, G. D., Hamilton, P. B., Hinz, F., & Hehanussa, P. E. (2006). An examination of species within the genus Surirella from the Malili Lakes, Sulawesi Island, Indonesia, with descriptions of 11 new taxa, *21*(1), 1–56. http://doi.org/10.1080/0269249X.2006.9705650

Brock, T. D. (1978). *Thermophilic Microorganisms and Life at High Temperatures*. New York : Springer-Verlag.

Campbell, K. A., Guido, D. M., Gautret, P., Foucher, F., Ramboz, C., & Westall, F. (2015). Geyserite in hot-spring siliceous sinter: Window on Earth's hottest terrestrial (paleo)environment and its extreme life. *Earth-Science Reviews*, *148*, 44–64. http://doi.org/10.1016/j.earscirev.2015.05.009

Campbell, K. A., Guido, D. M., John, D. A., Vikre, P. G., Rhys, D., & Hamilton, A. (2018). The Miocene Atastra Creek sinter (Bodie Hills volcanic field, California and Nevada): 4D evolution of a geomorphically intact siliceous hot spring deposit. *Journal of Volcanology and Geothermal Research*, (xxxx). http://doi.org/10.1016/j.jvolgeores.2018.12.006

Campbell, K. A., Rodgers, K. A., Brotheridge, J. M. A., & Browne, P. R. L. (2002). An unusual modern silica-carbonate sinter from Pavlova spring, Ngatamariki, New Zealand. *Sedimentology*, *49*(4), 835–854. http://doi.org/10.1046/j.1365-3091.2002.00473.x

Cruz, V. (2016). Hidrogeoquímica de aguas termales y mineralizadas de la zona de Jaraña, Paratía, Puno. In *Congreso Peruano de*

Geología, 18 (p. 5). Lima: Sociedad Geológica del Perú.

Cunneen, R., & Sillitoe, R. H. (1989). Paleozoic hot spring sinter in the Drummond Basin, Queensland, Australia. *Economic Geology*, *84*, 135–142.

Fournier, R., Kennedy, B. M., Aoki, M., & Thompson, J. M. (1994). Correlation of gold in siliceous sinters with 3He/4He in hot spring waters of Yellowstone National Park, *58*(24), 5401–5419.

Guido, D., de Barrio, R., & Schalamuk, I. (2002). La Marciana Jurassic sinter — implications for exploration for epithermal precious-metal deposits in Deseado Massif, southern Patagonia, Argentina La Marciana Jurassic sinter — implications for exploration for epithermal precious-m. *Applied Earth Science*, *111*(2), 106–113. http://doi.org/10.1179/aes.2002.111.2.106

Guido, D. M., & Campbell, K. A. (2011). Jurassic hot spring deposits of the Deseado Massif (Patagonia, Argentina): Characteristics and controls on regional distribution. *Journal of Volcanology and Geothermal Research*, *203*(1–2), 35–47. http://doi.org/10.1016/j.jvolgeores.2011.04.001

Guido, D. M., & Campbell, K. A. (2018). Upper Jurassic travertine at El Macanudo, Argentine Patagonia: A fossil geothermal field modified by hydrothermal silicification and acid overprinting. *Geological Magazine*, *155*(6), 1394–1412. http://doi.org/10.1017/S0016756817000498

Guido, D. M., Channing, A., Campbell, K. A., & Zamuner, A. (2010). Jurassic geothermal landscapes and fossil ecosystems at San Agustin, Patagonia, Argentina. *Journal of the Geological Society*, *167*(1), 11–20. http://doi.org/10.1144/0016-76492009-109

Gutscher, M. A., Olivet, J. L., Aslanian, D., Eissen, J. P., & Maury, R. (1999). The “lost Inca Plateau”: Cause of flat subduction beneath Peru? *Earth and Planetary Science Letters*, *171*(3), 335–341. http://doi.org/10.1016/S0012-821X(99)00153-3

Hamilton, A., Campbell, K., Rowland, J., & Browne, P. (2017). The Kohuamuri siliceous sinter as a vector for epithermal mineralisation, Coromandel Volcanic Zone, New Zealand. *Mineralium Deposita*, *52*(2), 181–196. http://doi.org/10.1007/s00126-016-0658-8

Hamilton, A. R., Campbell, K. A., Rowland, J. V, Barker, S., & Guido, D. M. (2019). Fossilised geothermal surface features of the Whitianga Volcanic Centre (Miocene), Coromandel Volcanic Zone, New Zealand : Controls and characteristics. *Journal of Volcanology and Geothermal Research*, *381*, 209–226. http://doi.org/10.1016/j.jvolgeores.2019.06.009

Handley, K. M., Campbell, K. A., Mountain, B. W., & Browne, P. R. L. (2005). Abiotic–biotic controls on the origin and development of spicular sinter: in situ growth experiments, Champagne Pool, Waiotapu, New Zealand. *Geobiology*, *3*(2), 93–114.

Hayashi, K. (2013). Oxygen Isotope Study of Silica Sinter from the Osorezan. *International Journal of Geosciences*, *4*(December), 1438–1446. http://doi.org/10.4236/ijg.2013.410141

INGEMMET. (2018). GEOCATMIN. Retrieved from http://geocatmin.ingemmet.gob.pe/

Kanellopoulos, C., Mitropoulos, P., Valsami-Jones, E., & Voudouris, P. (2017). A new terrestrial active mineralizing hydrothermal system associated with ore-bearing travertines in Greece (northern Euboea Island and Sperchios area). *Journal of Geochemical Exploration*, *179*(May), 9–24. http://doi.org/10.1016/j.gexplo.2017.05.003

Lynne, B. Y. (2012). Mapping vent to distal-apron hot spring paleo-flow pathways using siliceous sinter architecture. *Geothermics*, *43*, 3–24. http://doi.org/10.1016/j.geothermics.2012.01.004

Lynne, B. Y., & Campbell, K. A. (2003). Diagenetic transformations (opal-A to quartz) of low- and mid-temperature microbial textures in siliceous hot-spring deposits, Taupo Volcanic Zone, New Zealand. *Canadian Journal of Earth Sciences*, *40*(11), 1679–1696. http://doi.org/10.1139/e03-064

Lynne, B. Y., Campbell, K. A., Moore, J. N., & Browne, P. R. L. (2005). Diagenesis of 1900-year-old siliceous sinter (opal-A to quartz) at Opal Mound, Roosevelt Hot Springs, Utah, U.S.A. *Sedimentary Geology*, *179*(3–4), 249–278. http://doi.org/10.1016/j.sedgeo.2005.05.012

Nicholson, K., & Parker, R. J. (1990). Geothermal sinter towards a diagnostic signature and a sinter geothermometer. In *12th New Zealand Geothermal Workshop* (pp. 97–102).

Nicolau, C. B. (2013). *Physico-Chemical and Environmental Controls on Siliceous Sinter Formation At the High-Altitude El Tatio Geothermal Field, Northern Chile*. Universidad de Chile.

Okrugin, V. M., Andreeva, E. D., Chubarov, V. M., Yablokova, D. A., & Shishkanova, K. O. (2015). Sulfides of the Modern Kamchatka Hydrothermal Systems, (April), 19–25.

Pajuelo, D., Condorhuaman, A., Cruz, V., & Zegarra, E. (2016). Características geológicas de la zona geotérmica de Pinaya- región Puno (pp. 1–4). Lima-Perú: XVIII Congreso Peruano de Geología.

Pentecost A. (2005). *Travertine*. *Springer* (1st ed.). Berlin, Heidelberg, New York: Springer Netherlands. http://doi.org/10.1007/1-4020-3606-X

Renaut, R. W., & Jones, B. (2000). Microbial Precipitates Around Continental Hot Springs and Geysers. In R. E. Riding & S. M. Awramik (Eds.), *Microbial Sediments* (pp. 187–195). Springer-Verlag Berlin Heidelberg.

Renaut, R. W., & Jones, B. (2011). Hydrothermal Environments, Terrestrial, 467–479. http://doi.org/https://doi.org/10.1007/978-1-4020-9212-1_114

Rosenbaum, G., Giles, D., Saxon, M., Betts, P. G., Weinberg, R. F., & Duboz, C. (2005). Subduction of the Nazca Ridge and the Inca Plateau: Insights into the formation of ore deposits in Peru. *Earth and Planetary Science Letters*, *239*(1–2), 18–32.

http://doi.org/10.1016/j.epsl.2005.08.003

Rowland, J. V., & Simmons, stuart F. (2012). Hydrologic, Magmatic, and Tectonic Controls on Hydrothermal Flow, Taupo Volcanic Zone, New Zealand : Implications for the Formation of Epithermal Vein Deposits. *Economic Geology*, *107*, 427–457. http://doi.org/0361-0128/12/4018/427.31

Smith, D. J. (2008). *From Slab To Sinter: the Magmatic-Hydrothermal System of Savo Volcano, Solomon Islands*. University of Leicester. Retrieved from http://hdl.handle.net/2381/8207

Stolz, J. F. (2000). Structure of Microbial Mats and Biofilms. In R. E. Riding & S. M. Awramik (Eds.), *Microbial Sediments* (pp. 1–8). Springer-Verlag Berlin Heidelberg.

Takashima, C., Kano, A., Naganuma, T., & Tazaki, K. (2008). Laminated iron texture by iron-oxidizing bacteria in a calcite travertine. *Geomicrobiology Journal*, *25*(3–4), 193–202. http://doi.org/10.1080/01490450802081887

Tassara, A. (2005). Interaction between the Nazca and South American plates and formation of the Altiplano Puna plateau: Review of a flexural analysis along the Andean margin (15° 34°S). *Tectonophysics*, *399*(1–4), 39–57. http://doi.org/10.1016/j.tecto.2004.12.014

Terra, J. G. S., Spadini, A. R., França, A. B., Leite, C., Zambonato, E. E., Costa, L., … Maria, S. (2010). *Classificações Clássicas De Rochas Carbonáticas*. *B. Geoci. Petrobras, Rio de Janeiro* (Vol. 18). Rio de Janeiro.

Valdivieso, L. G. (2015). *Proyecto de exploración sabina , comparación con los depósitos Arasi y Pinaya , franja metalogenética XXI , sur del Perú*. Lima-Perú.

Warren, J. (2016). *Evaporites* (2nd ed.). Springer International Publishing. http://doi.org/10.1007/978-3-319-13512-0